Imaging of near-surface heterogeneities by scattered elastic waves

GEOPHYSICS, VOL. 80, NO. 4 (JULY-AUGUST 2015); P. A83–A88, 5 FIGS., 1 TABLE.
10.1190/GEO2014-0416.1

Imaging of near-surface heterogeneities by scattered elastic waves

Abdulaziz M. Almuhaidib[1] and M. Nafi Toksöz[2]

ABSTRACT

We have developed an elastic reverse time migration (RTM) approach for imaging near-surface heterogeneities, such as karst features, using scattered waves (e.g., body to P-, S-, and surface waves). Knowledge of location and strength of the scatterers helps in seismic imaging, survey planning, and geotechnical site characterization. To model seismic wave propagation for RTM, we use an elastic staggered-grid finite-difference scheme. The scattered body-to-surface waves provide optimal illumination and wavenumber coverage of the near surface as they travel horizontally along the free surface. We tested the elastic RTM approach on synthetic data simulated using a finite-difference solver and found it to be robust.

INTRODUCTION

Near-surface objects, such as karst features, act as strong scatterers and affect the quality of seismic data used for subsurface imaging. Determining, locating, and imaging of such features are important for deep and shallow reflection imaging for resource exploration and geotechnical site characterization, respectively. In this paper, we describe a method of imaging the scattering objects using scattered body and surface waves.

In general, depth migration algorithms are categorized as ray-based (e.g., high-frequency asymptotic methods such as Kirchhoff and beam migration) and wave-equation-based (e.g., one-way and two-way wave-equation-based migrations). The concept based on two-way wave equation migration is known as reverse time migration (RTM) (Baysal et al., 1983; Loewenthal and Mufti, 1983; McMechan, 1983; Whitmore, 1983). Although RTM is computationally expensive, it is more attractive than other imaging algorithms because it can handle multiple arrivals and overturned waves, and it has no restrictions with respect to the complexity of the velocity model or the dip of the structure.

RTM schemes based on the acoustic-wave equation have been more widely used than elastic RTM for imaging complex geologic structures due to the lower computational cost. The earth, however, is elastic, and the data recorded in the field contain all wave types, including P-wave, S-wave, converted, etc. In recent years, there has been more interest in exploiting all the information carried by mode-converted seismic data by using elastic RTM. Sun et al. (2006) introduce a modified RTM approach of transmitted P-to-S converted (PS) waves for salt-flank imaging. Their approach separates the wavefield into pure mode PP- and PS-waves, and the extrapolation is performed using the scalar wave equation with the corresponding P- and S-wave velocities. A similar strategy is proposed by Xiao and Leaney (2010) for salt-flank imaging with vertical seismic profiling, local elastic RTM, and using the vector wave equation to extrapolate the separated PP- and PS-waves. Shang et al. (2012) use teleseismic transmitted P- and S-waves recorded on the surface to perform passive-source RTM to reconstruct steeply dipping interfaces, an approach superior to traditional receiver-function analysis in complex geologic environments.

To address the problem of imaging near-surface scatterers, several studies have formulated solutions of the inverse scattering problems. Blonk et al. (1995), Blonk and Herman (1996), Ernst et al. (2002), and Kaslilar (2007) use a perturbation method based on the Born approximation (single scattering). These methods have difficulties when dealing with large and high-contrast heterogeneities that violate the Born approximation. Campman et al. (2005, 2006) use an inverse scattering approach based on an integral-equation formulation to image the near-surface heterogeneities, but they assume that scattering takes place immediately under the receivers. Other methods, based on solving integral equations using the method of moments, can handle strong contrast and large heterogeneities and can take into account multiple scattering (Riyanti and Herman, 2005; Campman and Riyanti, 2007). However, these

Manuscript received by the Editor 9 September 2014; revised manuscript received 10 February 2015; published online 10 June 2015; corrected version published online 23 June 2015.
[1]Formerly Massachusetts Institute of Technology, Earth Resources Laboratory, Cambridge, Massachusetts, USA; presently Saudi Aramco, EXPEC Advanced Research Center, Dhahran, Saudi Arabia. E-mail: muhaidib@alum.mit.edu.
[2]Massachusetts Institute of Technology, Earth Resources Laboratory, Cambridge, Massachusetts, USA. E-mail: toksoz@mit.edu.

methods are restricted to laterally homogeneous background media consisting of horizontal layers.

In this paper, we present a prestack elastic RTM for locating and imaging near-surface scatterers. The main idea is to separate the near-surface scattered waves from the total recorded wavefield and to use the scattered waves for receiver wavefield extrapolation. An elastic staggered-grid finite-difference scheme is used for wavefield extrapolation (Virieux, 1986; Levander, 1988). For the P-wave separation (e.g., divergence of the wavefield), the finite-difference scheme can be used to calculate the spatial derivatives of the measured wavefields (Dellinger and Etgen, 1990). The P-wave separation is derived after wavefield extrapolation and is subjected to a crosscorrelation-type imaging condition (Claerbout, 1971). The stresses and particle velocities are migrated simultaneously by solving the first-order elastic-wave equation. To the best of our knowledge, this is the first attempt to image the near surface by incorporating the body waves and the full-scattered wavefield. We test the proposed elastic RTM approach on data simulated with an elastic finite-difference scheme.

METHODOLOGY

The main idea underlying elastic RTM for imaging near-surface scatterers is to back project the near-surface scattered waves (e.g., body to P-, S-, and surface waves) until they are in-phase (e.g., time of conversion) with the incident waves at the scatterer locations (Figure 1). In the shot-profile domain, the image is constructed by (1) forward propagating the reference wavefield (modeled data with the estimated source wavelet), (2) back propagating the scattered wavefield (recorded multicomponent data) as boundary conditions, and (3) separating the reference and scattered wavefields into P-wave components (i.e., divergence of the wavefield) before the imaging condition is applied at each image location. The reference and scattered wavefields are also referred to as the source and receiver wavefields, respectively.

The multicomponent source and receiver wavefields are extrapolated in time by solving the seismic elastic-wave equation in isotropic elastic media as

$$\rho\frac{\partial^2\mathbf{u}}{\partial t^2}-(\lambda+2\mu)\nabla(\nabla\cdot\mathbf{u})+\mu\nabla\times(\nabla\times\mathbf{u})=\mathbf{f}, \quad (1)$$

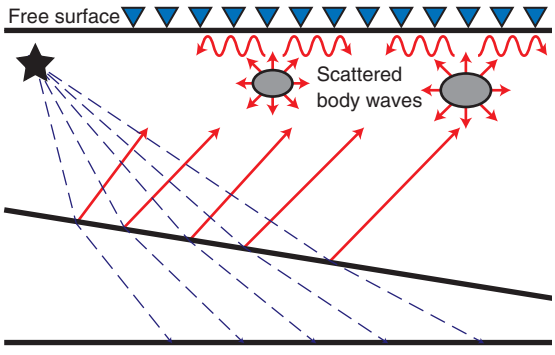

Figure 1. Schematic earth model showing the reflected waves (long red arrows) as a source for the reference or source wavefield and the receiver wavefield composed of near-surface scattered waves as demonstrated by the short and wavy red arrows (corresponding to scattered body and surface waves, respectively).

where ρ is density, λ and μ are Lamé parameters, $\mathbf{u}$ is the displacement vector, and $\mathbf{f}$ is a force term (e.g., source wavelet or receiver wavefield injected as a boundary condition). This equation can be separated into scalar and vector potentials by the Helmholtz decomposition, which applies to the vector field $\mathbf{u}$:

$$\mathbf{u}=\nabla\phi+\nabla\times\varphi, \quad (2)$$

where ϕ and φ are the scalar and vector potentials of the wavefield $\mathbf{u}$, respectively. Substituting equation 2 into equation 1 and applying vector identities gives the equations for the P-wave potential:

$$\nabla^2\phi-\frac{1}{\alpha^2}\frac{\partial^2}{\partial t^2}\phi=0 \quad (3)$$

and the S-wave potential:

$$\nabla^2\varphi-\frac{1}{\beta^2}\frac{\partial^2}{\partial t^2}\varphi=0, \quad (4)$$

where φ is one component of the vector potential in equation 2, and α and β are the P- and S-wave velocities, respectively.

For reverse time continuation, the data (i.e., the separated scattered wavefield) are reversed at the corresponding receiver locations and injected as sources (e.g., v_x- and v_z-components) into the computational domain using an elastic-wave equation solver. The P-wave mode is separated at each wavefield-extrapolation step by taking the divergence of the wavefield $\nabla\cdot\mathbf{u}$, and an imaging condition

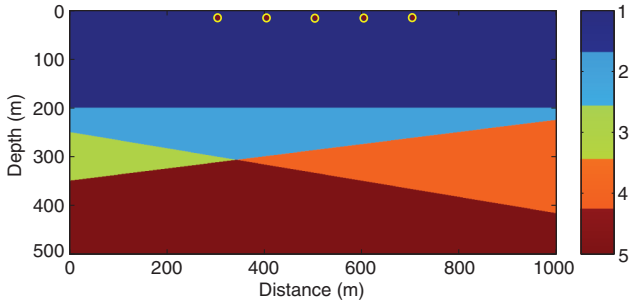

Figure 2. Synthetic earth model with multiple dipping layers and five circular scatterers (red circles near the free surface). The scatterers are located at 15-m depth; each one is 10 m in diameter and has an impedance contrast corresponding to 0.36. The color scale (on the right side) and associated numbers refer to material properties given in Table 1.

Table 1. Material properties (P-wave velocity α, S-wave velocity β, and density ρ) of the model shown in Figure 2.

Material index	α (m/s)	β (m/s)	ρ (kg/m^3)
1 — dark blue	1800	1000	1750
2 — blue	2200	1200	1900
3 — green	2500	1300	2000
4 — orange	2700	1400	2100
5 — red	3000	1500	2250

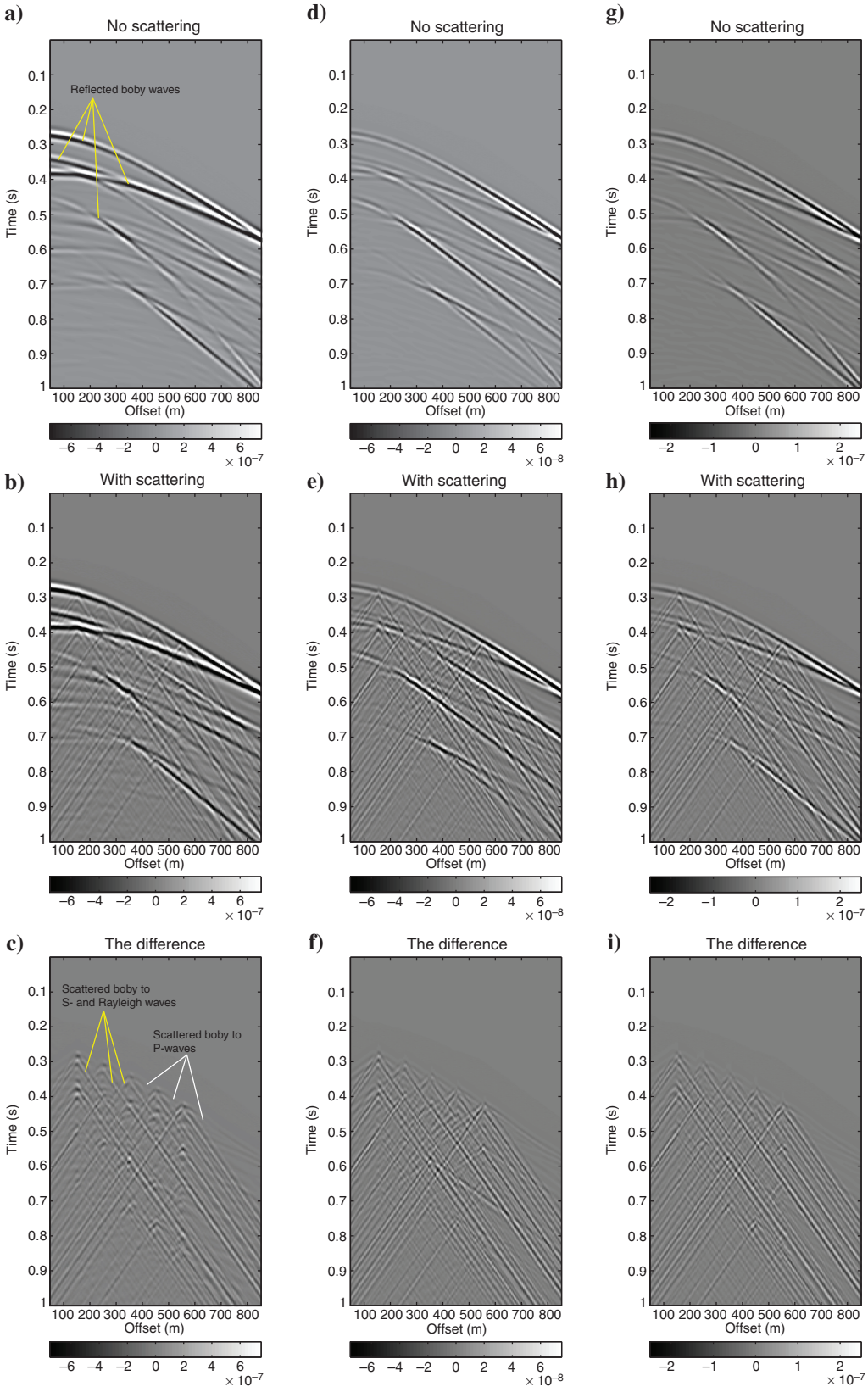

Figure 3. Finite-difference simulations showing the (a-c) v_z-component, (d-f) divergence, and (g-i) curl; panels (a, d, g) show the reference wavefield simulated using the model without scatterers, panels (b, e, h) show the total wavefield simulated using the model with scatterers, and panels (c, f, i) show the scattered wavefield. The color scales indicate amplitudes. The source is located at $(x, z) = (150\ , 0\ \text{m})$.

is applied to form an image of the scatterers. The zero-lag cross-correlation imaging condition is defined as follows:

$$m(x) = \sum_{\text{shots}} \int_0^{t_{\max}} S(x,t)R(x,t)dt, \tag{5}$$

where m is the value of the migration image at a spatial location x and S and R are the P-wave modes of the forward- and time-reversed wavefields. The imaging condition computes the scalar product of the two wavefields at each time step and summation over all time levels and shot locations.

For simplifying the imaging condition, the S-waves are not included by taking the divergence of the wavefield. However, the P-wave component of the Rayleigh waves and upcoming mode-converted reflections (e.g., SP, SSP, SPP, and PSP) are incorporated in the imaging condition. The reflections of not only P- but also S-waves from the deeper dipping interfaces provide superior angle coverage, and the use of Rayleigh waves plays a key role in broadening the illumination angle to 180°.

NUMERICAL TESTS

In this section, we demonstrate the application of elastic RTM to synthetic data calculated using elastic finite-difference modeling. We consider a 2D earth model with multiple dipping layers and five scatterers embedded in the uppermost layer (Figure 2). The scatterers are located at 15-m depth below the free surface, and each has a 10-m diameter and an impedance contrast corresponding to 0.36. The material properties are given in Table 1. A vertical point source is used with a Ricker wavelet and 30-Hz center frequency (approximately 75-Hz maximum frequency). The simulations are carried for 19 sources located at the surface with 50-m space intervals. The receivers are at the surface and placed at intervals of 1 m. To image the near-surface scatterers, we assume the reflected body-wave arrivals as the reference wavefield (i.e., the source wave-

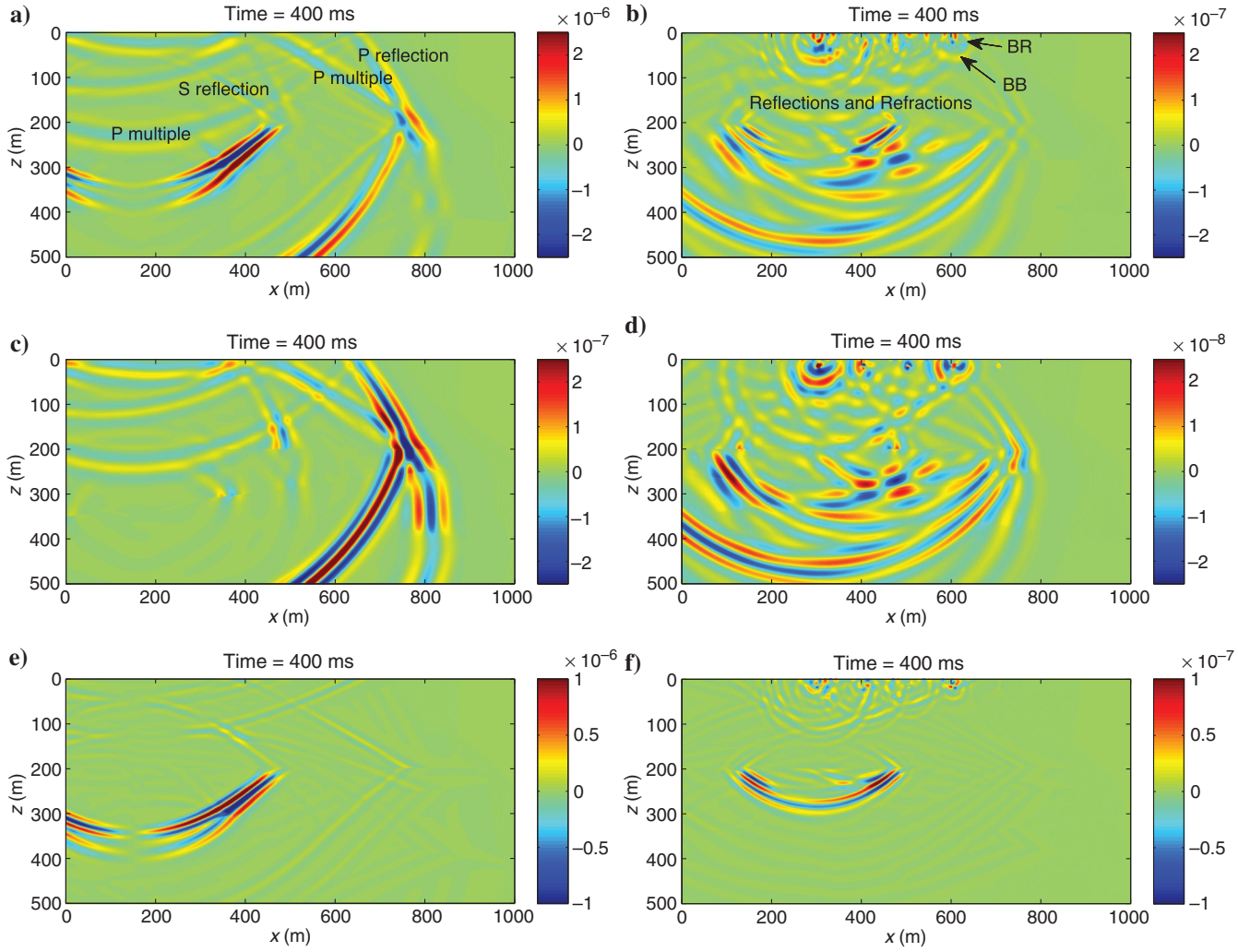

Figure 4. (a and c) Snapshots of the v_z-component, (e and b) divergence, and (d and f) curl of the (a, e, and d) reference and (c, b, and f) scattered wavefields. The seismic source is located at $(x, z) = (150, 0$ m). The source of scattering is reflected or refracted body waves. The scatterers excite primary, shear and, also, surface waves due to the proximity to the free surface. BB and BR in panel (c) refer to scattered body-to-body and body-to-Rayleigh waves, respectively. Note that the scattered surface-to-surface waves are removed. For clarity, the color scales of the scattered wavefield plots are enhanced by an order of magnitude compared with their corresponding incident wavefield plots.

field), as the direct body and surface waves are modeled and removed during the wavefield extrapolation. This implies that the interfaces (i.e., reflectors) act as seismic sources (Figure 1) for the incident waves on the scatterers. The *receiver wavefield* (i.e., reflected body waves scattered to body and surface waves) is obtained by first modeling and then subtracting the reference wavefield from the total wavefield (Figure 3).

In Figure 4, snapshots of the v_z-component, divergence (P-waves), and curl (S-waves) of the incident and scattered waves are shown. The snapshots clearly show the wavefield decomposition into P- and S-waves by applying the divergence and curl operators. However, it is difficult to identify the separated phases in the shot-gather domain in the case of surface receivers. This is due to mode conversion occurring right at the free surface where the receivers are placed. For example, we can observe weak S-waves in the shot-gather domain (the curl of the wavefield as shown in Figure 3i) recorded with similar slopes to the P-wave arrivals. These wave phases are scattered P-waves converted to S-waves right at the free-surface boundary. The same is also true in the case of the scattered S-wave arrivals converted to P-waves at the free surface and recorded with similar slopes to the S-wave phases (as shown by the divergence of the wavefield in Figure 3f).

The near-surface scatterers' image is formed by applying the imaging condition (equation 5) to the P-wave components of the extrapolated forward reference and backward-scattered wavefields stored at each time step (Figure 5a). The wavefield extrapolation is carried out using a velocity model with no a priori information of the scatterers, and the image is constructed when the near-surface scattered waves are in-phase with the incident waves at the scatterer locations. All the scatterers are imaged and located accurately. However, the image can be distorted due to limited illumination aperture (Figure 5b) in case the recorded scattered wavefield is simulated with an absorbing boundary at the surface, in which free-surface multiples and scattered body-to-surface waves are not included in the imaging process.

Because the reflected signal is used as the source wavefield, the subsurface interfaces as expected, are not accurately imaged by RTM. The only exceptions, however, are very weak scattered body-to-body waves reflected from the deep interfaces and recorded on the surface. These recorded phases can slightly contribute to imaging the deep reflectors. In general, artifacts in the RTM image can be due to many factors, including the imaging condition, injection of the receiver wavefield as a boundary condition for backward extrapolation, and the one-sided coverage of the receivers.

Previously (Almuhaidib and Toksöz, 2014), we have studied the near-surface scattering of body-to-surface waves and demonstrate the effects of source characteristics and near-surface perturbations (e.g., volume and interface heterogeneities). Body-to-body scattered waves, in general, require illumination from all angles (i.e., receivers surrounding the computational domain) to achieve true relative amplitude migration. In contrast, scattered body-to-surface waves travel horizontally along the free surface and attenuate less with distance than body waves. Therefore, they are recorded by all receivers on the surface and provide optimal illumination of the near-surface layers. However, because the amplitude of surface waves decays exponentially with depth, only near-surface heterogeneities that are close to the free surface (e.g., shallower than one wavelength) can be illuminated and imaged by the scattered body-to-surface waves. As a result, the intensity of the imaged scatterers with scattered surface waves decreases with depth, and therefore, body-to-body-wave scattering contributes more to the image.

DISCUSSION

The results presented in this paper demonstrate the feasibility of imaging and locating near-surface heterogeneities using waves scat-

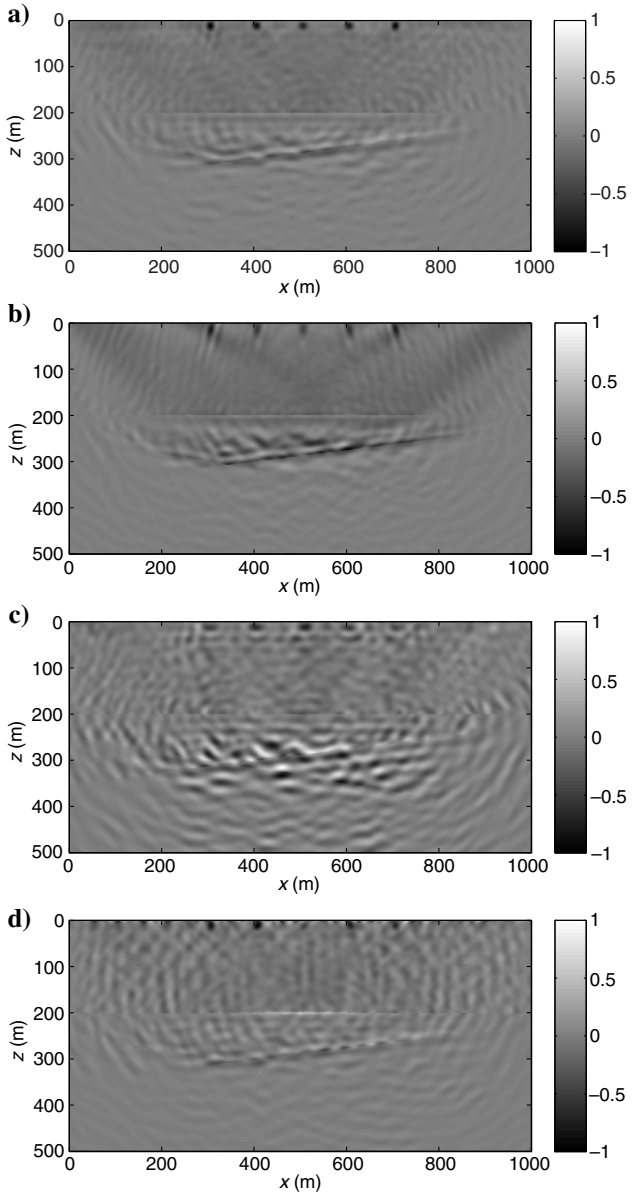

Figure 5. Elastic RTM of near-surface scattered waves with receivers placed on the surface; panel (a) shows imaging the near-surface scattered body to P-, S-, and surface waves, panel (b) shows imaging without free-surface multiples and only scattered body-to-body waves are included (e.g., the recorded scattered wavefield is modeled with an absorbing boundary at the surface), panel (c) shows the same as panel (a) but with almost 10% error in the upper layer's velocity ($\alpha = 2000$ m/s and $\beta = 1100$ m/s instead of $\alpha = 1800$ m/s and $\beta = 1000$ m/s), panel (d) shows imaging with the back scattered Rayleigh-to-Rayleigh waves included. The color scales indicate normalized amplitudes.

tered at the near surface. There are, however, some remaining questions that may cause difficulties in field data application and need to be answered. In this section, we will address two important questions.

The first question is how to obtain the velocity model for wavefield extrapolation. Indeed, a precise depth image depends on the ability to accurately estimate the subsurface velocity model especially for field data. As shown in Figure 5c, small errors in the velocity model can significantly defocus the image results. In such cases, an extension of our approach to update the velocity model based on least-squares migration or waveform inversion would be essential.

The second question is how to perform the wavefield separation in case the velocity model is not accurately estimated. The answer to this question is that scattered body-to-surface waves exhibit different slopes than body-wave reflections, which make them easier to separate (e.g., using a velocity filter) for subsurface imaging. In a previous study, Almuhaidib and Toksöz, 2015), we develop a data-based approach to separate the scattered surface waves based on laterally varying local slopes. In the case of incomplete separation of backscattered Rayleigh-to-Rayleigh waves, the image can be distorted with artifacts as shown in Figure 5d. These wave types, however, are excited with large amplitudes and low frequencies, which can form the basis for their suppression to reduce the image artifacts.

CONCLUSION

In this paper, we have presented a prestack elastic (RTM) approach for imaging near-surface scatterers. The image is constructed by forward propagating the source wavefield (e.g., reflected body waves) and back projecting the receiver wavefield (e.g., near-surface scattered body to P-, S-, and surface waves) before a zero-lag imaging condition is applied. For simplicity, we have used only the P-wave components (e.g., divergence of the wavefields). The wavefield extrapolation is performed using an elastic finite-difference scheme. We have shown, using synthetic data, that the elastic RTM of near-surface scattered waves constructs a reliable depth image of the near-surface scatterers. The elastic RTM scheme preserves the relative amplitude because all wave propagation losses, including mode conversions, are properly taken into account. The scattered body-to-surface waves travel horizontally along the free surface, and they provide optimal illumination and wavenumber coverage of the near surface when combined with nearly vertical body waves. However, because the surface waves decay exponentially with depth, the heterogeneities that are close to the free surface are better illuminated and imaged by the scattered surface waves. The proposed imaging approach can be easily extended to 3D problems, and it can find important applications in seismic imaging, survey planning, and geotechnical site characterization.

ACKNOWLEDGMENTS

We thank the Saudi Aramco and ERL founding members for supporting this research. During part of this study, M. N. Toksöz was partially supported by the Kuwait Foundation for the Advancement of Sciences and Kuwait-MIT Center for Natural Resources and the Environment. We are grateful to the Associate Editor and three anonymous reviewers for their helpful reviews and comments that significantly improved the manuscript.

REFERENCES

Almuhaidib, A. M., and M. N. Toksöz, 2014, Numerical modeling of elastic wave scattering by near-surface heterogeneities: Geophysics, **79**, no. 4, T199–T217, doi: 10.1190/geo2013-0208.1.

Almuhaidib, A. M., and M. N. Toksöz, 2015, Suppression of near-surface scattered body-to-surface waves: A steerable and non-linear filtering approach: Geophysical Prospecting, doi: 10.1111/1365-2478.12275.

Baysal, E., D. D. Kosloff, and J. W. Sherwood, 1983, Reverse time migration: Geophysics, **48**, 1514–1524, doi: 10.1190/1.1441434.

Blonk, B., and G. C. Herman, 1996, Removal of scattered surface waves using multicomponent seismic data: Geophysics, **61**, 1483–1488, doi: 10.1190/1.1444073.

Blonk, B., G. C. Herman, and G. G. Drijkoningen, 1995, An elastodynamic inverse scattering method for removing scattered surface waves from field data: Geophysics, **60**, 1897–1905, doi: 10.1190/1.1443921.

Campman, X. H., G. C. Herman, and E. Muyzert, 2006, Suppressing near-receiver scattered waves from seismic land data: Geophysics, **71**, no. 4, S121–S128, doi: 10.1190/1.2204965.

Campman, X., and C. D. Riyanti, 2007, Non-linear inversion of scattered seismic surface waves: Geophysical Journal International, **171**, 1118–1125, doi: 10.1111/j.1365-246X.2007.03557.x.

Campman, X. H., K. van Wijk, J. A. Scales, and G. C. Herman, 2005, Imaging and suppressing near-receiver scattered surface waves: Geophysics, **70**, no. 2, V21–V29, doi: 10.1190/1.1884831.

Claerbout, J. F., 1971, Toward a unified theory of reflector mapping: Geophysics, **36**, 467–481, doi: 10.1190/1.1440185.

Dellinger, J., and J. Etgen, 1990, Wave-field separation in two-dimensional anisotropic media: Geophysics, **55**, 914–919, doi: 10.1190/1.1442906.

Ernst, F. E., G. C. Herman, and A. Ditzel, 2002, Removal of scattered guided waves from seismic data: Geophysics, **67**, 1240–1248, doi: 10.1190/1.1500386.

Kaslilar, A., 2007, Inverse scattering of surface waves: Imaging of near-surface heterogeneities: Geophysical Journal International, **171**, 352–367, doi: 10.1111/j.1365-246X.2007.03524.x.

Levander, A. R., 1988, Fourth-order finite-difference P-SV seismograms: Geophysics, **53**, 1425–1436, doi: 10.1190/1.1442422.

Loewenthal, D., and I. R. Mufti, 1983, Reversed time migration in spatial frequency domain: Geophysics, **48**, 627–635, doi: 10.1190/1.1441493.

McMechan, G. A., 1983, Migration by extrapolation of time-dependent boundary values: Geophysical Prospecting, **31**, 413–420, doi: 10.1111/j.1365-2478.1983.tb01060.x.

Riyanti, C. D., and G. C. Herman, 2005, Three-dimensional elastic scattering by near-surface heterogeneities: Geophysical Journal International, **160**, 609–620, doi: 10.1111/j.1365-246X.2005.02492.x.

Shang, X., M. V. Hoop, and R. D. Hilst, 2012, Beyond receiver functions: Passive source reverse time migration and inverse scattering of converted waves: Geophysical Research Letters, **39**, L15308, doi: 10.1029/2012GL052289.

Sun, R., G. A. McMechan, C.-S. Lee, J. Chow, and C.-H. Chen, 2006, Prestack scalar reverse-time depth migration of 3D elastic seismic data: Geophysics, **71**, no. 5, S199–S207, doi: 10.1190/1.2227519.

Virieux, J., 1986, P-SV wave propagation in heterogeneous media: Velocity-stress finite-difference method: Geophysics, **51**, 889–901, doi: 10.1190/1.1442147.

Whitmore, N., 1983, Iterative depth migration by backward time propagation: Presented at 53rd Annual International Meeting, SEG, Expanded Abstracts, 382–385.

Xiao, X., and W. S. Leaney, 2010, Local vertical seismic profiling (VSP) elastic reverse-time migration and migration resolution: Salt-flank imaging with transmitted P-to-S waves: Geophysics, **75**, no. 2, S35–S49, doi: 10.1190/1.3309460.